

See discussions, stats, and author profiles for this publication at: <https://www.researchgate.net/publication/2729863>

Active Flow Control Using a Reduced Order Model and Optimum Control

Article · February 1997

DOI: 10.2514/6.1996-1946 · Source: CiteSeer

CITATIONS

35

READS

72

3 authors, including:



J. Peraire

Massachusetts Institute of Technology

329 PUBLICATIONS 12,437 CITATIONS

[SEE PROFILE](#)

Some of the authors of this publication are also working on these related projects:



Towards high-order Large-Eddy Simulation for complex turbulent flows [View project](#)



MIT Hall Thruster Plume Modeling Research [View project](#)

Active Flow Control using a Reduced Order Model and Optimum Control

K.Y. Tang, W.R. Graham*, J. Peraire

Computational Aerospace Sciences Laboratory

MIT Department of Aeronautics and Astronautics

Abstract

An approach to developing active control strategies for separated flows is presented. The methodology proposed is applied to the incompressible unsteady wake flow behind a circular cylinder at $Re = 100$. Control action is achieved via cylinder rotation. Low order models which are amenable to control and which incorporate the full non-linear dynamics are developed using the Proper Orthogonal Decomposition (POD) technique. These models are generated from data provided by numerical simulation. The model predictions are found to be capable of describing control-induced departures from stationary conditions, making it feasible to envisage employing them for model-based control of the vortex-shedding flow. The use of these models and the resulting optimal control results are discussed.

1 Introduction

The idea of controlling an unstable or unsteady fluid flow in order to optimize its characteristics in some way is highly attractive, and has a wide range of potential applications. However, the implementation of this concept is contingent upon the availability of a model of the flow which is suitable for control system design. Thus, to date, applications have been restricted to situations where it is possible to derive simple, sometimes heuristic, models describing the flow behavior and control system action. In many cases of interest though, such models are not available *a-priori*, and one is faced with the prospect of using expensive full-scale numerical simulations in the control design process. In this paper we describe an alternative approach, whereby a simple, low-order system model is derived numerically from the Navier-Stokes simulation data and then used as the basis for control system design.

2 Navier-Stokes Numerical Simulation of the Cylinder Flow

We consider two-dimensional, incompressible, viscous flow past a circular cylinder at Reynolds numbers where vortex shedding occurs. The large scale separation region and the global unsteadiness of this flow are typical features of applications where flow control is potentially beneficial. One can envisage a variety of possible control objectives, such

*Visiting from the Dep. of Eng., University of Cambridge, Cambridge, England

Copyright ©1996 American Institute of Aeronautics and Astronautics, Inc. All rights reserved.

as, the minimization of drag, the minimization of transverse force fluctuation, or the reduction of wake unsteadiness.

The incompressible Navier-Stokes equations are discretized in time via a three step projection method (Chorin [1]) and in space using a Galerkin finite element approximation (Donea et al [2] and Zienkiewicz et al [3]).

$$\frac{\mathbf{u}^* - \mathbf{u}^{(n)}}{\Delta t} = -\mathbf{u}^{(n)} \cdot \nabla \mathbf{u}^{(n)} + \nu \nabla^2 \mathbf{u}^{(n)} \quad (1)$$

$$\nabla^2 p^{(n)} = \rho \frac{\nabla \cdot \mathbf{u}^*}{\Delta t} \quad (2)$$

$$\frac{\mathbf{u}^{(n+1)} - \mathbf{u}^*}{\Delta t} = -\frac{\nabla p^{(n)}}{\rho} \quad (3)$$

Here $\mathbf{u}^{(n)}$ consists of the x- and y- components of velocity and $p^{(n)}$ represents the pressure. The superscripts denote the time level of the variables, ρ and ν are the fluid density and kinematic viscosity respectively, and Δt is the time step.

Steps (1) and (3) together represent an explicit time-stepping solution to the Navier-Stokes equations;

$$\frac{\partial \mathbf{u}}{\partial t} = -\mathbf{u} \cdot \nabla \mathbf{u} - \frac{\nabla p}{\rho} + \nu \nabla^2 \mathbf{u} \quad (4)$$

while the pressure calculation in step (2) enforces the incompressibility condition $\nabla \cdot \mathbf{u} = 0$.

In the absence of upwind spatial differencing, or added artificial viscosity, the formulation described here would suffer from the well-known numerical instability problems associated with the discretization of the convective term. Such difficulties may be avoided by replacing the right hand side of equation (1) by

$$\frac{\mathbf{u}^* - \mathbf{u}^n}{\Delta t} = -(\mathbf{u}^n \cdot \nabla) \mathbf{u}^n + \frac{1}{Re} \nabla^2 \mathbf{u}^n + \frac{\Delta t}{2} \nabla \cdot [(\mathbf{u}^n \otimes \mathbf{u}^n) \cdot \nabla] \mathbf{u}^n \quad (5)$$

where \otimes denotes the dyadic product. The additional term plays the role of an added artificial viscosity which is only active in the streamline direction (Christie et al [4], Hughes et al [5], Donea [6]) and despite having only a higher order effect, due to the presence of Δt , it is found to be sufficient to stabilize the numerical solution.

The spatial domain is discretized into a mesh of triangular elements, and linear shape functions $N_i(\mathbf{x})$ [$\mathbf{x} = (x, y)$] are

defined for each node i of the mesh. Figure (1) shows the finite element mesh, consisting of 6650 triangles and 3401 vertices, used for the computations reported in this paper. The requirements that $N_i(\mathbf{x})$ be one at the node i , zero at all the other nodes, and be piecewise linear in x and y -coordinates over each triangular element are sufficient to specify it uniquely. These shape functions may be used to approximate the problem variables \mathbf{u} and p in a piecewise linear fashion

$$\mathbf{u} \approx \sum_i \mathbf{u}_i N_i(\mathbf{x}), \quad p(\mathbf{x}) \approx \sum_i p_i N_i(\mathbf{x}) \quad (6)$$

where the summation extends over the total number of vertices, and \mathbf{u}_i and p_i denote the values of the velocity and pressure at the mesh node i . It is noted the present algorithm allows for equal interpolations for \mathbf{u} and p since the pressure is determined directly from the Poisson equation (2).

The finite element spatial discretization thus yields three matrix equations involving the finite element mass matrix for equations (1) and (3) and the finite element Laplacian matrix for equation (2). The solution of these equations represents our numerical approximation to the flow. Furthermore, due to the strongly local nature of the shape functions, the matrices in these equations are sparse, symmetric and positive definite, and amenable to efficient solution by iterative methods. Here a preconditioned conjugate gradient algorithm with a diagonal preconditioning matrix is employed.

The numerical flow solution for the non-rotating circular cylinder at a Reynold's number 100 is computed. A typical pressure contour plot of the resultant flow is presented in figure (2). The corresponding time history of the lift and drag coefficients are displayed in figure (3). The computed lift and drag coefficients are in good agreement with the results of previous experimental and computational (Simo et al [7]) investigations.

3 Reduced Order Model for a Non-rotating Cylinder

For illustrative purposes, we derive in this section a reduced order model for the non-rotating cylinder flow. The low order model is derived from the numerical simulation by performing a proper orthogonal decomposition on the data (Sirovich [8] and Berkooz et al [9]), thereby generating a set of spatial functions which are used as a basis for a Galerkin projection of the Navier-Stokes equations.

Given a set of velocity fields corresponding to N discrete times, $\mathbf{u}_j, j = 1 \dots N$, the "snapshot" form of the POD (Sirovich [8]) generates N basis functions ('modes') of the form, $\Psi_i = \sum_j \alpha_{ij} \mathbf{u}_j$, which are mutually orthogonal and optimal in terms of their ability to represent the flow kinetic energy. For each mode Ψ_i the coefficients α_{ij} are the components of the i -th eigenvector of the correlation matrix

$$K_{ij} = (\mathbf{u}_i - \mathbf{u}_m, \mathbf{u}_j - \mathbf{u}_m) \quad (7)$$

and the corresponding eigenvector represents the energy associated with that mode. In equation (7), \mathbf{a}, \mathbf{b} denotes the standard inner product of two vector fields \mathbf{a}, \mathbf{b} and $\mathbf{u}_m(\mathbf{x})$ is the flow mean value obtained as the arithmetic average of the snapshots. The Galerkin projection

$$\left(\frac{\partial \mathbf{u}}{\partial t} + \mathbf{u} \cdot \nabla \mathbf{u} + \frac{\nabla p}{\rho} - \nu \nabla^2 \mathbf{u}, \Psi_i \right) = 0 \quad (8)$$

combined with the representation,

$$\mathbf{u} = \mathbf{u}_m + \sum_j y_j(t) \Psi_j(\mathbf{x}) \quad (9)$$

yields the N coupled ordinary differential equations:

$$\frac{dy_i}{dt} = a_i + \sum_j b_{ij} y_j + \sum_j \sum_k c_{ijk} y_j y_k \quad (10)$$

Note that the pressure term does not appear in equation (10) because the basis functions Ψ_i are divergence-free by construction and therefore

$$(\Psi_i, \nabla p) = \int_{\Gamma} p \Psi_i \cdot \mathbf{n} ds \quad (11)$$

where Γ is the domain boundary. The above boundary integral is equal to zero, since $\Psi_i \cdot \mathbf{n} = 0$ on the inflow, lateral far-field boundaries and the cylinder surface, and $p = 0$ on outflow far-field boundary.

Thus, given a set of initial conditions $y_i(0)$, the time evolution of the basis function amplitudes may be calculated from these equations. For illustrative purposes, snapshots are taken after the stationary periodic motion of the Navier-Stokes simulation has been fully established. Figure (4) shows the eigenvalue spectrum of the correlation matrix formed from a set of 15 snapshots, obtained at regular intervals over two vortex shedding periods. Clearly, most of the fluctuation energy is captured by the first two modes alone, and if six modes are taken the remaining eigenvalues account for less than 0.1 of the unsteadiness in the snapshots. The decomposition of the flow achieved here is thus highly efficient. These results are in agreement with those of Deane et al [10], and the associated basis functions also correspond satisfactorily. Velocity contours for the first four are plotted in figures (5) to (8). Note the pairing of similar patterns, shifted spatially, a result of the convective nature of the flow.

Figure (9) shows a comparison of the evolution of the mode amplitudes obtained firstly by integrating equations (10), and secondly by projecting the solution obtained from the Navier Stokes simulation onto the Ψ_i . Excellent agreement is obtained between the simulation and the low order model prediction. Similar results to those reported here were found by Deane et al [10].

4 Inclusion of Cylinder Rotation

To introduce control into the problem, we consider cylinder rotation as a means of actuation. A similar control idea

has been suggested by Burns et al [11]. Two approaches are proposed to address this problem. The first, which we call the ‘‘Control Function Method’’, is motivated by the desirability of having homogeneous boundary conditions on the basis functions used in the Galerkin projection, and involves the removal of the inhomogeneous boundary condition by including a suitably chosen function (the ‘‘control function’’) in the expansion of the velocity field. The second, the ‘‘Penalty Method’’ retains the POD basis functions in their original form, and imposes the inhomogeneous boundary condition on the cylinder in a weak sense when performing the Galerkin projection. Both formulations are formally valid, but yield qualitatively different low order models, and it is thus of interest to compare their performance.

4.1 The Control Function Method

A convenient way to generate a control function is to take the flow solution generated via simulation for the desired motion of the boundary. Here, this is simply the velocity field generated by a steady cylinder rotation with angular velocity $\gamma = 1$ and a zero velocity and constant pressure at the far-field boundary. The velocity contours of the control function are shown in figure (10). Note that this flow solution approximates a potential vortex. Denoting this solution by $\mathbf{u}_c(\mathbf{x})$, the modified snapshot set is now

$$\mathbf{u}(\mathbf{x}, t^k) - \gamma(t^k)\mathbf{u}_c(\mathbf{x}) \quad (12)$$

and the mean flow and basis functions are obtained from this modified set in the usual way. The Ψ_i thus generated have zero velocity on the cylinder surface, and the velocity expansion

$$\mathbf{u} = \mathbf{u}_m + \gamma(t)\mathbf{u}_c + \sum_j y_j(t)\Psi_j(\mathbf{x}) \quad (13)$$

where the term $\gamma(t)\mathbf{u}_c$ satisfies the non-homogeneous velocity boundary condition on the rotating cylinder. The Galerkin projection then yields:

$$\frac{dy_i}{dt} = \sum_j a_{ij}y_j + \sum_j \sum_k b_{ijk}y_j y_k + \sum_j \gamma c_{ij}y_j + \gamma d_i + \gamma^2 f_i + g_i \frac{d\gamma}{dt} + h_i, \quad i = 1 \dots N \quad (14)$$

where y_i represents the amplitude of mode i , γ denotes the *control*, and the coefficients a_{ij} , b_{ijk} , c_{ij} , d_i , f_i , g_i and h_i , are constant. Thus, given a known control $\gamma(t)$, the above equations can be numerically integrated in time for any suitable set of initial conditions $\{y_i(0), i = 1 \dots N\}$.

4.2 The Penalty Method

In this approach the essential boundary condition is enforced in an integral, ‘‘weak’’ fashion. The velocity on the cylinder surface is written as

$$\mathbf{u} = \gamma R \mathbf{e}_\theta - \epsilon \frac{\partial \mathbf{u}}{\partial n} \quad (15)$$

where R is the cylinder radius, \mathbf{e}_θ the unit tangent vector and ϵ a small parameter. We can then replace our essential boundary condition with the alternative, derivative boundary condition

$$\frac{\partial \mathbf{u}}{\partial n} = -\frac{\mathbf{u} - \gamma R \mathbf{e}_\theta}{\epsilon} \quad (16)$$

which may be imposed in a weak sense via surface integral terms in the Galerkin projection (Zienkiewicz et al [12]). As $\epsilon \rightarrow 0$, \mathbf{u} on the cylinder boundary will converge to the original boundary condition. Essentially, this approach may be thought of as imposing $\mathbf{u} = \gamma R \mathbf{e}_\theta$ a distance ϵ into the fluid, and reducing that distance until a satisfactory solution is obtained.

In this case, on performing the Galerkin projection, we obtain

$$\frac{dy_i}{dt} = a_i + \sum_{j=1}^N b_{ij}y_j + \sum_{j=1}^N \sum_{k=1}^N c_{ijk}y_j y_k + d_i \gamma \quad (17)$$

Note that, even though our Ψ_i are non-zero on the cylinder surface, $\Psi \cdot \mathbf{n} = 0$ still; hence the continued absence of the pressure term. As with the control function formulation, equation (17) may be integrated forwards in time, subject to a set of initial conditions and specified $\gamma(t)$, to yield predictions for the mode amplitudes.

4.3 Generalized Basis Functions

It was found that the basis functions obtained from the non-rotating Navier-Stokes simulations were not capable of producing a good prediction of the flow when the cylinder rotation was included. Since this problem is associated with the unphysical coupling of conditions at the cylinder with conditions downstream, we seek a method of generating snapshots which de-couples these elements. In essence, we need to vary the phase of the vortex shedding at the cylinder, so that the unsteady dynamics of the system are reflected in the snapshots.

In order to carry out this system identification procedure a cylinder rotation of the form,

$$\gamma = \gamma_o \sin\left[\frac{2\pi t}{T_1} + A \pi \sin\left(\frac{2\pi t}{T_2}\right)\right] \quad (18)$$

essentially a varying frequency sinusoid, or ‘chirp’ is imposed. Here we consider $\gamma_o = 2$, $T_1 = 6$, $A = 1$, $T_2 = 48$ which yields excitation from around half to twice the shedding frequency as shown in figure (11).

The chirp applied after the stationary ‘locked-on’ flow condition corresponding to a cylinder rotation given by $\gamma_o =$

$2, T_1 = 6, A = 0$. After the chirp is started 75 snapshots are taken at time intervals of 0.64, and these are used to form the correlation matrix in equation (7).

The eigenvalue spectrum of the correlation matrix is shown in figure (12). Clearly, the varying-frequency cylinder rotation results in a flow with many more degrees of freedom (based on energy distribution) than the steady-state shedding. Figures (13) to (15) show some velocity contour plots of the obtained basis functions. From these it may be seen that our goal of generating basis functions capable of providing a more "physical" description of the flow has, at least to some extent, been attained. The presence of nearly frozen patterns convecting downstream may be accounted for by modes like those of figure (13), while other modes are dominated by local behavior around the cylinder (e.g. figure 14). Any changes in the mean flow due to the varying excitation also appear in the basis functions (e.g. figure 15).

5 The Optimum Control Problem

In this section we consider the problem of determining a control $\gamma(t)$ satisfying an initial condition $\gamma(0) = \gamma_0$ that will minimize a given cost function. Of interest here, are cost functions which can be written in the following general form

$$E(\mathbf{y}, \gamma) = \int_0^T f(\mathbf{y}, \gamma) dt \quad (19)$$

where \mathbf{y} is a vector whose i -th component is the mode amplitude y_i . An iterative algorithm can be devised to evaluate $\gamma(t)$ from a sequence of updates starting from an initial guess γ^0 and corresponding solution \mathbf{y}^0 . For each iteration a gradient function $G(\mathbf{y}^k, \gamma^k)$ satisfying

$$\delta E = G(\mathbf{y}^k, \gamma^k) \delta \gamma \quad (20)$$

is evaluated. Then, a straightforward steepest descent update

$$\gamma^{k+1} = \gamma^k - \alpha_k G^k \quad (21)$$

guarantees that $E(\gamma^{k+1}) \leq E(\gamma^k)$ for a sufficiently small scalar α_k . The iteration process is stopped when the magnitude of the gradient function becomes smaller than a prescribed tolerance. Clearly, more sophisticated update algorithms can be used.

5.1 Continuum Formulation

An efficient calculation of the gradient function in equation (20) can be accomplished using the ideas of Optimum Control Theory (Lions [13] and Pironneau [14]). In this approach the equation set (14) is regarded as a constraint on

the problem variables y_i and γ . Introducing co-state variables $\{\phi^i, i = 1 \dots N\}$ the cost function in equation (19) for the Control Function method is replaced by

$$E(\mathbf{y}, \gamma) = \int_0^T f(\mathbf{y}, \gamma) dt - \int_0^T \phi^i \left(\frac{dy_i}{dt} - a_{ij} y_j - b_{ijk} y_j y_k - \gamma c_{ij} y_j - \gamma d_i - \gamma^2 f_i - g_i \frac{d\gamma}{dt} - h_i \right) dt \quad (22)$$

Clearly, if we restrict ourselves to functions y_i satisfying equations (14), the minimization of equation (22) is equivalent to the minimization of (19) since the additional term is identically zero for arbitrary ϕ^i functions.

Taking the first variation of the above equation we can write

$$\begin{aligned} \delta E(\mathbf{y}, \gamma) = & \int_0^T \left(\frac{\partial f}{\partial y_i} \delta y_i + \frac{\partial f}{\partial \gamma} \delta \gamma \right) dt - \\ & \int_0^T \phi^i \left(\frac{d\delta y_i}{dt} - a_{ij} \delta y_j - (b_{ijk} + b_{ij}) y_j \delta y_k - \right. \\ & \left. \gamma c_{ij} \delta y_j - c_{ij} y_j \delta \gamma - d_i \delta \gamma - 2\gamma f_i \delta \gamma - g_i \frac{d\delta \gamma}{dt} \right) dt \end{aligned} \quad (23)$$

which after integration by parts and rearranging leads to

$$\begin{aligned} \delta E(\mathbf{y}, \gamma) = & \int_0^T \left(\frac{d\phi^i}{dt} + [a_{ij} + \gamma c_{ij} + (b_{ski} + b_{ijk}) y_k] \phi^j \right. \\ & + \frac{\partial f}{\partial y_i} \delta y_i dt + \int_0^T \left(g_i \frac{d\phi^i}{dt} + [c_{ij} y_j + d_i + 2\gamma f_i] \phi^i \right. \\ & \left. + \frac{\partial f}{\partial \gamma} \right) \delta \gamma dt - [\phi^i \delta y_i]_0^T - [g_i \phi^i \delta \gamma]_0^T \end{aligned} \quad (24)$$

Since initial conditions are given on y^i and γ we consider only variations such that $\delta y^i(0) = 0$ and $\delta \gamma(0) = 0$. Therefore, if the functions ϕ^i solve the following problem

$$\frac{d\phi^i}{dt} = A_{ij} \phi^j - \frac{\partial f}{\partial y_i}, \quad \phi^i(T) = 0, \quad i = 1 \dots N \quad (25)$$

where $A_{ij} = -[a_{ij} + \gamma c_{ij} + (b_{ski} + b_{ijk}) y_k]$, then equation (23) reduces to

$$\begin{aligned} \delta E(\mathbf{y}, \gamma) = & \int_0^T \left([g_i A_{ij} + c_{ij} y_j + d_i + 2\gamma f_i] \phi^i + \right. \\ & \left. \frac{\partial f}{\partial \gamma} - g_i \frac{\partial f}{\partial y_i} \right) \delta \gamma dt \end{aligned} \quad (26)$$

Note that the problem in equation (25) is a linear initial value problem that needs to be solved in reverse time for the N co-state functions $\phi^i(t)$. Once these are known, it is straightforward to evaluate δE for an arbitrary variation in the control $\delta \gamma$ using expression (26). Similar derivation for the Penalty method could be obtained.

5.2 The Discrete Problem

In the discrete case, integrals are replaced by summations and the unknown control function $\gamma(t)$ is parameterized using an expansion of the form

$$\gamma(t) \approx \gamma(0)(1 - \frac{t}{T}) + \sum_{m=1}^{N_d} \beta_m \sin(\frac{m\pi t}{2T}) \quad (27)$$

The vector β^k containing the N_d design variables β_m^k can therefore be updated using the discrete analogue of equation (21)

$$\beta^{k+1} = \beta^k - \alpha_k G^k \quad (28)$$

and the components G_m^k of the discrete gradient vector G^k are computed as

$$G_m^k = \Delta t \sum_{n=0}^{N_t} \{ [g_i A_{ji}^{kn} + c_{ji} y_j^{kn} + d_i + 2\gamma^{kn} f_i] \phi_i^{kn} + (\frac{\partial f}{\partial \gamma})^{kn} - g_i (\frac{\partial f}{\partial y_i})^{kn} \sin(\frac{m\pi n \Delta t}{2T}) \} \quad (29)$$

where the superscript n denotes time level and $N_t = T/\Delta t$.

6 Prediction of the Optimal Controller Using the ODE System

6.1 Performance Measures

The greater spread of energy in the chirp-excited snapshots implies a need for a greater number of basis functions in our low order model. Here we take 18, as a compromise between model complexity and flow description accuracy (around 98% of the unsteady energy in the snapshots is captured by the first 18 basis functions). Assessment of our results by comparing predicted and observed modal amplitudes is thus no longer practical and we seek to define more rigorous performance measures.

We consider three velocity fields; the “exact” field $\mathbf{u}(\mathbf{x}, t)$ produced by the numerical simulation, the projected field $\mathbf{u}_p(\mathbf{x}, t)$ and the predicted field $\hat{\mathbf{u}}(\mathbf{x}, t)$. The second of these is the result of projecting the exact solution onto the reduced approximation space:

$$\mathbf{u}_p(\mathbf{x}, t) = \mathbf{u}_m(\mathbf{x}) + \sum_{i=0}^N y_i(t) \Psi_i(\mathbf{x}) \quad (30)$$

with

$$y_i = (\mathbf{u} - \mathbf{u}_m, \Psi_i) \quad (31)$$

This differs from $\mathbf{u}(\mathbf{x}, t)$ because of the inability of the Ψ_i to reproduce $\mathbf{u} - \mathbf{u}_m$ perfectly. The predicted field,

$$\hat{\mathbf{u}}(\mathbf{x}, t) = \mathbf{u}_m(\mathbf{x}) + \sum_{i=1}^N \hat{y}_i(t) \Psi_i(\mathbf{x}) \quad (32)$$

differs further, in that the \hat{y}_i are the estimates obtained from the low order model, rather than exact values obtained by projection. In the control function formulation, the corresponding expressions are

$$\mathbf{u}_p(\mathbf{x}, t) = \mathbf{u}_m(\mathbf{x}) + \gamma(t) \mathbf{u}_c(\mathbf{x}) + \sum_{i=1}^N y_i(t) \Psi_i(\mathbf{x}) \quad (33)$$

with

$$y_i = (\mathbf{u} - \mathbf{u}_m - \gamma \mathbf{u}_c, \Psi_i) \quad (34)$$

and

$$\hat{\mathbf{u}}(\mathbf{x}, t) = \mathbf{u}_m(\mathbf{x}) + \gamma(t) \mathbf{u}_c(\mathbf{x}) + \sum_{i=1}^N \hat{y}_i(t) \Psi_i(\mathbf{x}) \quad (35)$$

Based on these velocity fields, we define two error measures. The projection error, E_p , is given by

$$E_p = \frac{(\mathbf{u} - \mathbf{u}_p, \mathbf{u} - \mathbf{u}_p)}{(\mathbf{u} - \mathbf{u}_m, \mathbf{u} - \mathbf{u}_m)} \quad (36)$$

and the prediction error, \hat{E} , by

$$\hat{E} = \frac{(\mathbf{u} - \hat{\mathbf{u}}, \mathbf{u} - \hat{\mathbf{u}})}{(\mathbf{u} - \mathbf{u}_m, \mathbf{u} - \mathbf{u}_m)} \quad (37)$$

The normalization is chosen on the (estimated) velocity fluctuation $\mathbf{u} - \mathbf{u}_m$ to avoid the numerical “swamping” effect of including the mean flow. Since \mathbf{u}_m is, to all intents and purposes, the same for the control function and penalty methods (it differs only in so far as the mean value of γ among the snapshots differs from zero) these measures will provide a valid basis for comparison.

Finally, we note that the orthogonality of the basis functions may be used to simplify equation (36);

$$E_p = \frac{(\mathbf{u} - \mathbf{u}_m, \mathbf{u} - \mathbf{u}_m) - \sum_{i=1}^N y_i^2}{(\mathbf{u} - \mathbf{u}_m, \mathbf{u} - \mathbf{u}_m)} \quad (38)$$

for the penalty method, and

$$E_p = \frac{1}{(\mathbf{u} - \mathbf{u}_m, \mathbf{u} - \mathbf{u}_m)} [(\mathbf{u} - \mathbf{u}_m, \mathbf{u} - \mathbf{u}_m) - \sum_{i=1}^N y_i^2 - \gamma^2 (\mathbf{u}_c, \mathbf{u}_c) - 2\gamma \sum_{i=1}^N y_i (\Psi_j, \mathbf{u}_c)] \quad (39)$$

for the control function method. This quantity, resulting as it does from the exact projection of the flow onto the basis functions, will always be less than or equal to \hat{E} .

6.2 Test Case

For our test case, we take as initial condition the stationary flow past the non-rotating cylinder, and derive the optimal control for a look-ahead time corresponding to about three vortex shedding periods ($T = 20$). The low order models used are those derived from the generalized basis function and the forward and backward time integrations are carried out using a fourth-order Runge-Kutta method.

The cost function was chosen to be

$$E(\mathbf{y}, \gamma) = \int_0^T \sum_i y_i^2 + e^{N(\gamma^2 - \gamma_{max}^2)} dt \quad (40)$$

Here we associate our desire to reduce the wake unsteadiness with the mode amplitudes, y_i . The optimal control calculation is performed with $N_d = 50$ in the parameterization of γ and is halted once the reduction in E is less than 5% of its current value. The constants governing the control expense, N and γ_{max} (see equation (4)) are taken to be 10 and 2 respectively.

Figures (16) and (17), for the Control and Penalty method respectively, show the optimized control action for this example. The prescribed rotation is clearly well bounded by our imposed limit $\pm\gamma_{max}$, and tends to be largest over the first half of the time interval. This reflects the fact that later control action tends to affect mode amplitudes beyond the look-ahead time T (due to delays associated with convection), and the optimal control thus sees no value in any effort here.

The test of the algorithm lies in whether the control achieves its objective minimization of the sum of the squared mode amplitudes. This quantity is plotted in Figures (18) and (19), from which it is clear that significant reduction is achieved by the calculated control action. Note that despite the fact that the optimal control action predicted by the two methods are different, the unsteadiness decrease predicted by the two models are similar.

7 Example on Control of a Real System

In this section we discuss the application of the optimal control formulations to control the flow in the full Navier-Stokes simulation. Given the limited predictive capability of the low order models developed, some form of periodic

re-initialization of the mode amplitude estimates, y_i , is necessary and here we assume this re-initialization to be performed with full knowledge of the flow field.

Our objective here is the minimization of the (estimated) wake unsteadiness, $\mathbf{u} - \mathbf{u}_m$, which translates to the minimization of the mode amplitudes. The model performance over approximately the first eighth of a vortex-shedding period is reasonable, and accordingly we choose to re-initialize our estimates of the mode amplitudes every 0.25 time units. As this will be too short an interval to see the effect of a control action on the wake unsteadiness, we specify a corresponding look-ahead time (T in the formulation of Section 5) of 10.0. Fifty design variables are used in the parameterization for $\gamma(t)$ and the values of N and γ_{max} are kept to be 10 and 2 respectively. (Broadly similar results to those presented here are found if N_d is reduced to 25, but further reduction to 8 degrades the control performance noticeably.) The cylinder angular velocity histories for the two methods are shown in figures (20) and (21). The unsteadiness level for the two methods are shown in figures (22) and (23).

Pressure contours at 40 time units for the Control Function Method and the Penalty Method are shown in figures (24) and (25) respectively. These figures can be compared with the pressure contours (time units = 40) for the non-rotating cylinder flow which started from the same initial condition (see figure 2). Notice that from the unsteadiness history of both methods, at 40 time units, the unsteadiness level for the Control Function method is approximately equal to 2.5 whereas the one for the penalty method is about 4. The effect of the magnitude of the unsteadiness for both methods can be clearly observed in the pressure contour plots. Notice that the vortex shedding far behind the cylinder for the Control Function method almost entirely disappear whereas the one for the Penalty method can still be observed.

The control history predicted by the two methods is very different. In the control function method, we observe a periodic coherent rotation whereas for the penalty method, the control action is far less regular and noticeably not centering at zero. We note that the predicted flow behavior of the two methods is also quite different. For the control function method the average unsteadiness level is lower than for the penalty method. However, higher frequency components are found in the flow when the control function method is used.

8 Concluding Remarks

In this paper we have presented investigations into the application of the low order models to control of the unsteadiness in the cylinder wake. Specifically, we have derived optimal control formulations for the control function method and the penalty method and applied them to the numerical flow simulation, demonstrating that it is possible to reduce the wake unsteadiness via this approach, as long as one can reset the model periodically. From our limited experience, it is not clear which of the two approaches is

preferable. It has also been found that a poor choice of basis functions for the low order model can negate the benefits of the control.

We conclude, then, that low order model-based control of this flow is possible, and that the level of unsteadiness in the cylinder wake can be reduced. However the degree of complexity of our control “system” is markedly greater than would originally be suggested from a consideration of the uncontrolled flow, and this leads us to the general conclusion that actively-controlled flows may, in general, exhibit many more significant degrees of freedom than their unforced counterparts. Furthermore, attempts to control the degrees of freedom participating at a given time may tend to push the flow into other regions of parameter space, and the low order model employed must be capable of describing these regions sufficiently well to enable successful control. Here we have found the best model to be one generated by a varying frequency “chirp” in the cylinder rotation rate.

This discussion raises the question of whether it is possible to have a low order model which describes the controlled flow to a high degree of accuracy, or whether attempts to generate such a model and apply it to control the flow will simply excite more and more degrees of freedom.

Acknowledgments

The authors wish to express their gratitude to Jim Paduano, Eric Feron, Kenny Breuer and Stuart Jacobson for their contributions to a number of helpful discussions. The partial support for this work provided by the Flight Information Tests Systems Branch at the NASA Dryden Research Center under grant NAG4-100 is also gratefully acknowledged.

References

- [1] A.J.Chorin. *Numerical Solution of the Navier-Stokes Equations*. Math. Comp., 23, 1969.
- [2] J.Donea, S.Giuliani, H.Laral, and L.Quartapelle. *Finite Element Solution of the Unsteady Navier-Stokes Equations by a Fractional Step Method*. Comp. Meth. Appl. Mech. Engng., pages 53–73, 1982.
- [3] O.C.Zienkiewicz, J.Szmelter, and J.Peraire. *Compressible and Incompressible Flow; an Algorithm for All Seasons*. Comp. Meth. in Appl. Mech. and Engng., 78:105–121, 1990.
- [4] I.Christie, D.F. Griffiths, A.R.Mitchell, and O.C.Zienkiewicz. *Finite Element Methods for Second Order Equations with Significant First Derivatives*. Internat. J. Numer. Methods Engrg., 10:1389–1396, 1976.
- [5] T.J.R. Hughes and A.Brooks. *A Multidimensional Upwind Scheme with No Cross-Wind Diffusion*. ASME, Vol 34, 1979.
- [6] J.Donea. *A Taylor-Galerkin method for convective transport problems*. Int. J. Numer. Methods Eng., 20:101–119, 1984.
- [7] J.C. Simo and F. Armero. *Unconditional stability and long-term behavior of transient algorithms for the incompressible Navier-Stokes and Euler equations*. Computer Methods in Applied Mech. and Eng. 111 (1994) 111–154.
- [8] L. Sirovich. *Turbulence and the dynamics of coherent structures, Part I – III* Quarterly of Applied Mathematics, Vol XLV, Number 3, October 1987, p. 573–582.
- [9] G. Berkooz, P. Holmes, J.L. Lumley. *The proper orthogonal decomposition in the analysis of turbulent flows* Annu. Rec. Fluid Mech. 1993, Vol 25, p. 539–75.
- [10] A.E. Deane, I.G. Kevrekidis, G.E. Karniadakis, S.A. Orszag. *Low-dimensional models for complex geometry flows: Application to grooved channels and circular cylinders* Phys. Fluids A 3 (10), October 1991, p.2337–54.
- [11] J.A. Burns, Y.-R. Ou. *Active control of vortex shedding* AIAA 94-0182.
- [12] O.C.Zienkiewicz and K.Morgan. *Finite elements and approximation*. Wiley, Chichester, 1972.
- [13] J.L. Lions. *Optimal Control of Systems Governed by Partial Differential Equations*. Springer-Verlag, New-York, 1971.
- [14] O. Pironneau. *Optimal Shape Design for Elliptic Systems*. Springer-Verlag, New-York, 1984.

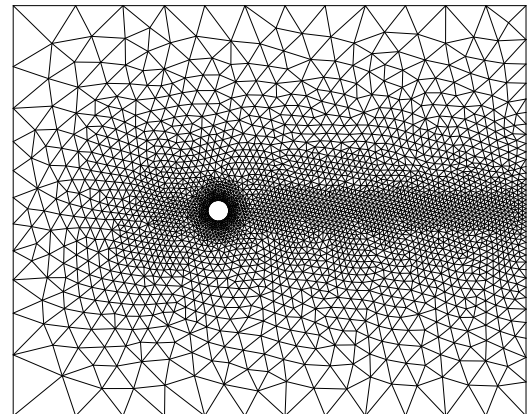


Figure 1: Mesh for the Circular Cylinder Flow

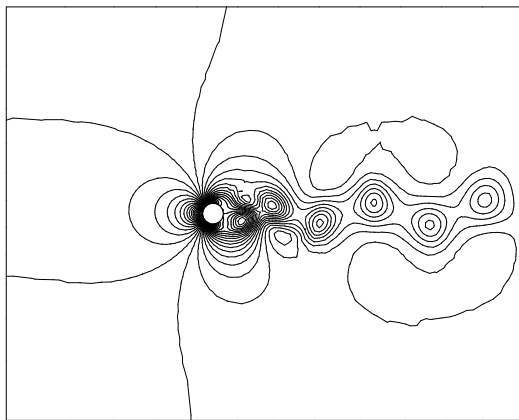


Figure 2: Pressure Contour

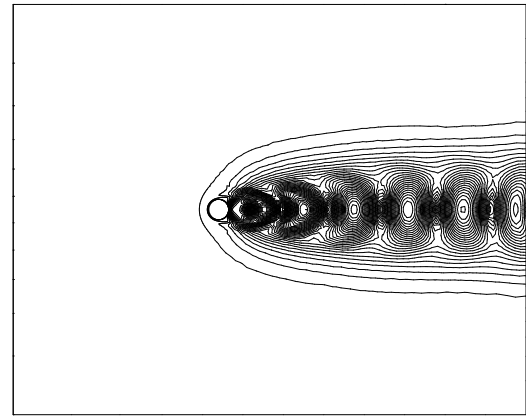


Figure 5: Velocity contours for the first mode

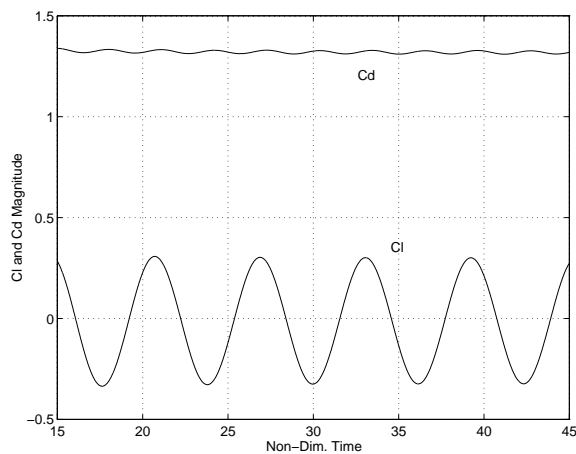


Figure 3: Coefficient of Lift and Drag History

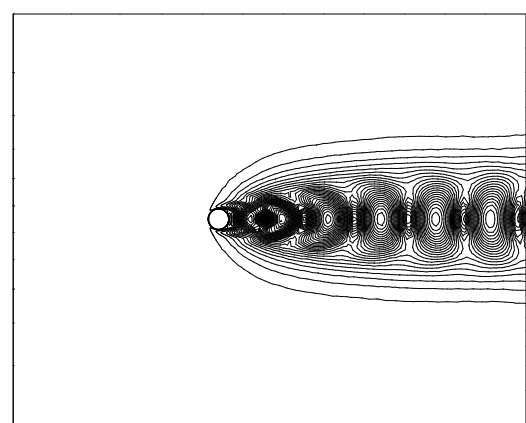


Figure 6: Velocity contours for the second mode

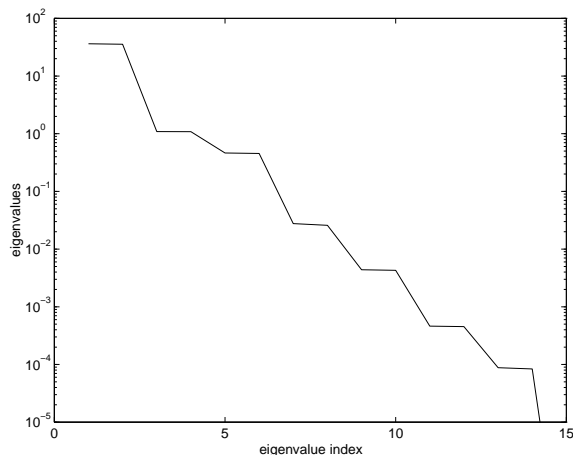


Figure 4: Eigenvalue spectrum

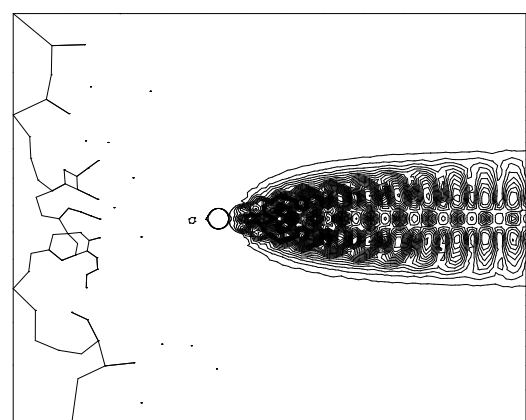


Figure 7: Velocity contours for the third mode

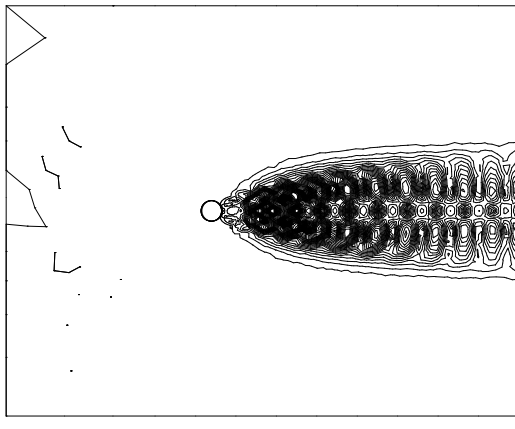


Figure 8: Velocity contours for the fourth mode

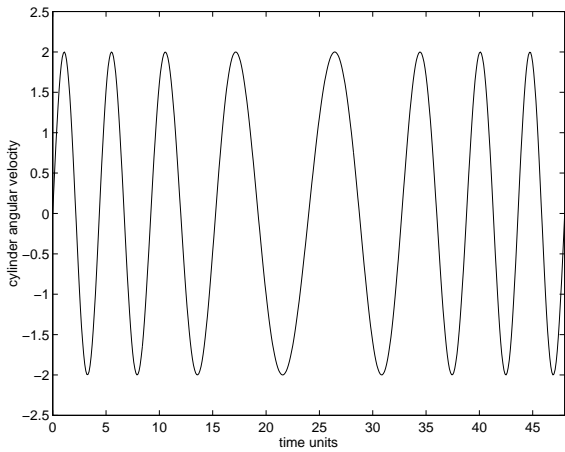


Figure 11: Chirp

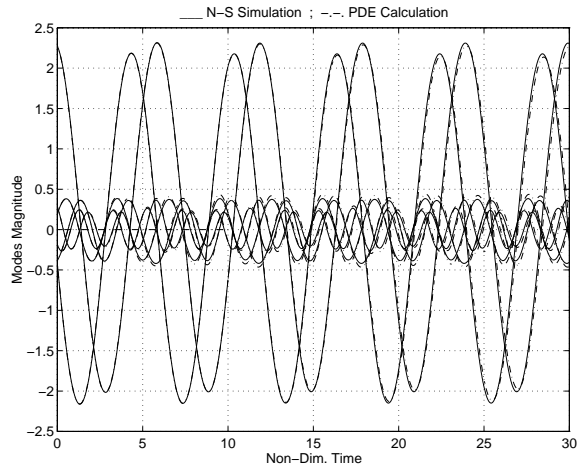


Figure 9: Comparision of N-S and POD Calculation

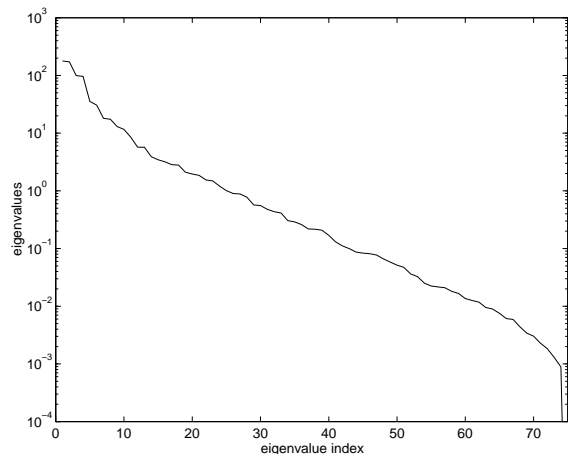


Figure 12: Eigenvalue spectrum

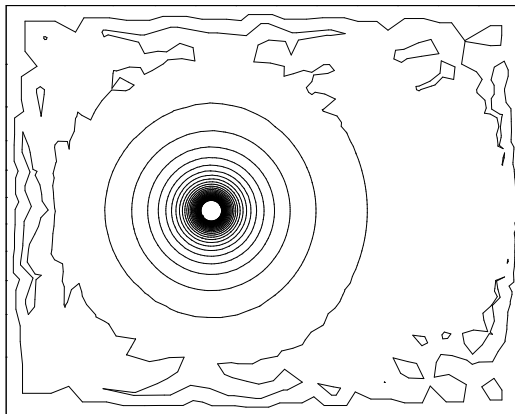


Figure 10: Velocity Contour of the Control Function

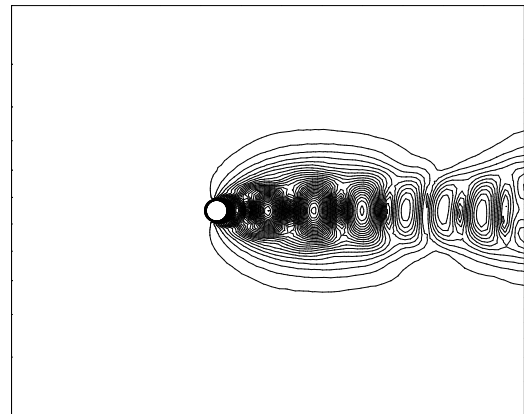


Figure 13: Velocity contours for the first mode

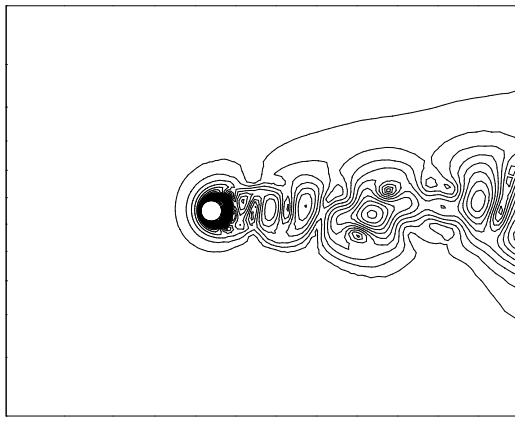


Figure 14: Velocity contours for the second mode

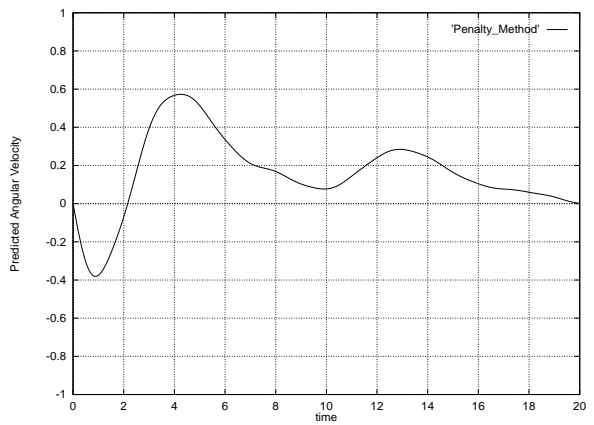


Figure 17: Optimized Control Action (Penalty Method)

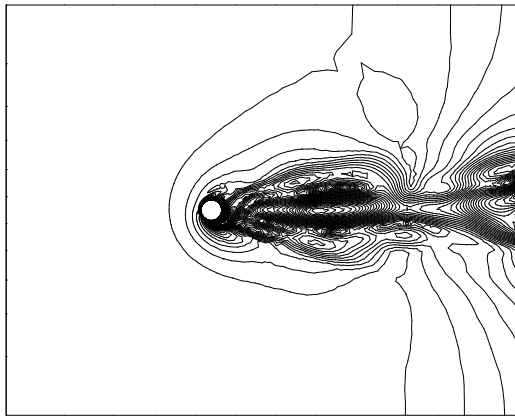


Figure 15: Velocity contours for the third mode

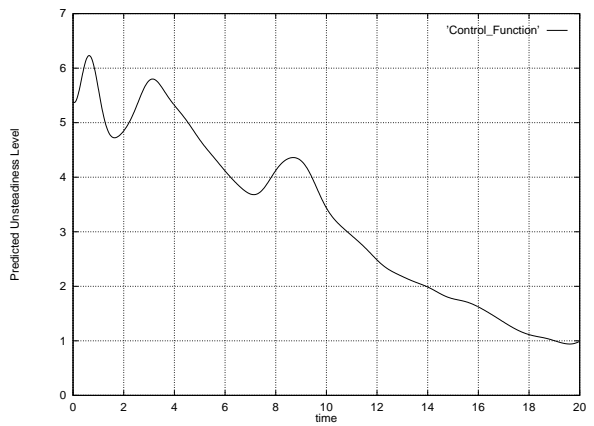


Figure 18: Unsteadiness History (Control Function)

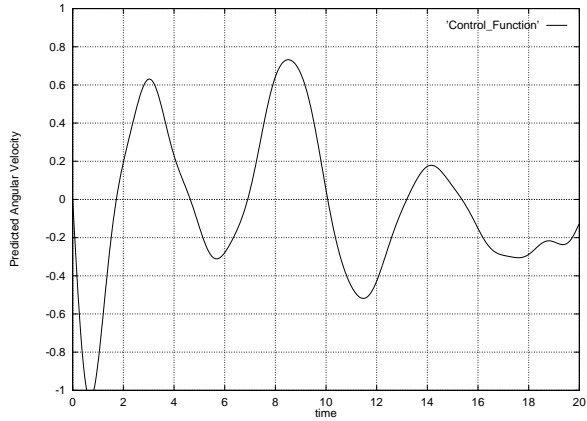


Figure 16: Optimized Control Action (Control Function)

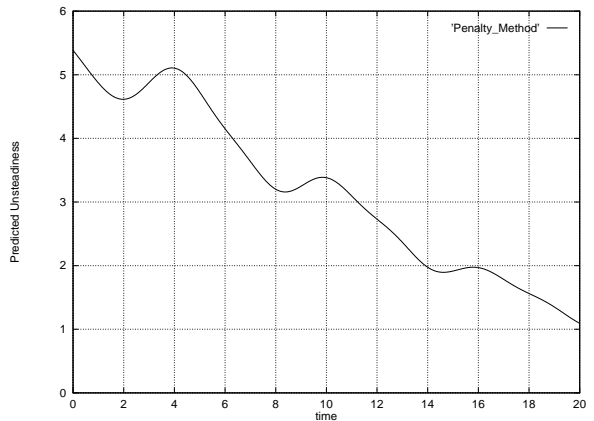


Figure 19: Unsteadiness History (Penalty Method)

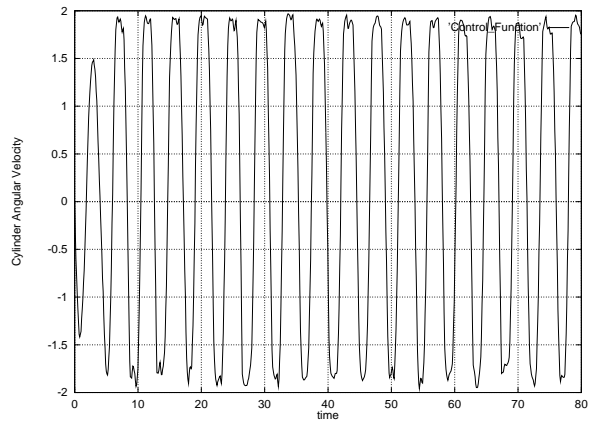


Figure 20: Optimized Control Action (Control Function)

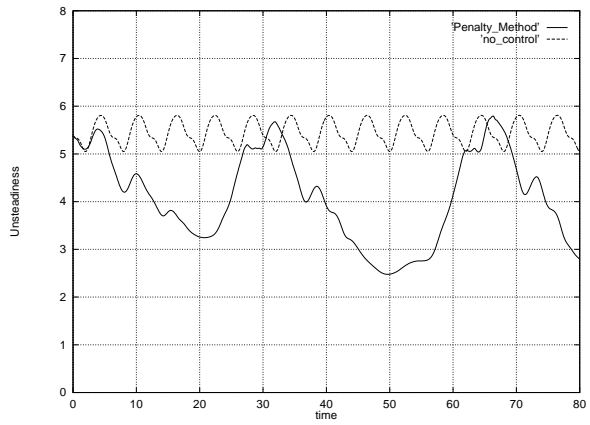


Figure 23: Unsteadiness History (Penalty Method)

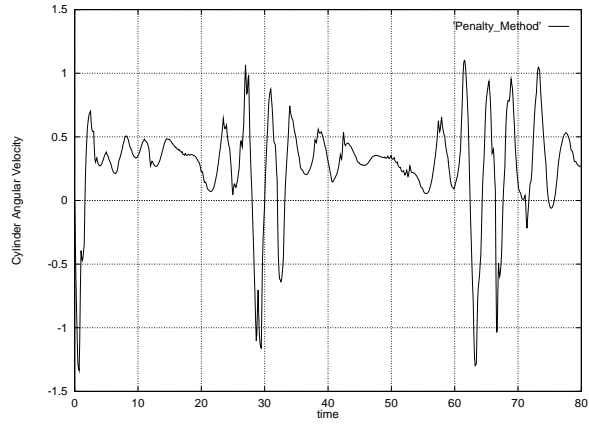


Figure 21: Optimized Control Action(Penalty Method)

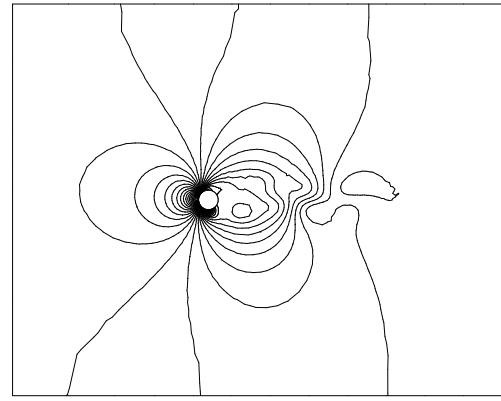


Figure 24: Pressure Contour (Control Function)

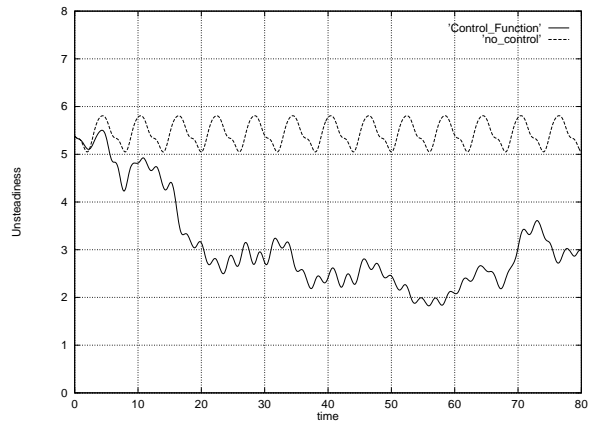


Figure 22: Unsteadiness History (Control Function)

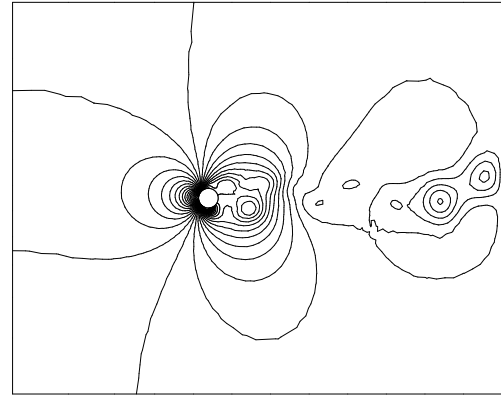


Figure 25: Pressure Contour (Penalty Method)